

# On the self-calibration capabilities of $\gamma$ -ray energy tracking arrays

S. Heil<sup>1</sup>, S. Paschalis<sup>2,a</sup>, and M. Petri<sup>1,2,b</sup>

<sup>1</sup> Institut für Kernphysik, Technische Universität Darmstadt, Darmstadt, Germany

<sup>2</sup> Department of Physics, University of York, York, UK

Received: 30 May 2018 / Revised: 24 August 2018

Published online: 12 October 2018

© The Author(s) 2018. This article is published with open access at Springerlink.com

Communicated by C. Ur

**Abstract.** Gamma-ray energy tracking arrays constitute the technological frontier of high-resolution  $\gamma$ -ray spectroscopy revolutionizing modern nuclear physics investigations. Their principle of operation lies on the precise reconstruction of the three-dimensional  $\gamma$ -ray interaction positions within the detector volume. The most common method to obtain these interaction points in real time is to compare the experimental signals against a reliable library of signals (signal basis) that maps the detector response as a function of the  $\gamma$ -ray interaction position. Obtaining a high-fidelity signal basis, however, remains a big technological challenge, which hinders the optimal operation of these state-of-the-art arrays. In this article, we propose a pioneering and notably simple method for generating experimentally a reliable signal basis. The proposed method enables the  $\gamma$ -ray tracking devices to perform a self-calibration of their position sensitive response *in situ*, opening up the way for reaching their optimum performance for the first time.

## 1 Introduction

For several decades, high resolution  $\gamma$ -ray spectroscopy, utilising High Purity Germanium (HPGe) detectors, has been key to our understanding of the atomic nucleus; indeed, many aspects of the strong nuclear force have been revealed by studying the de-excitation of atomic nuclei via  $\gamma$ -ray emission. Currently, the state-of-the-art in high-resolution  $\gamma$ -ray spectroscopy for nuclear physics experiments is the development of HPGe  $\gamma$ -ray energy tracking arrays. These arrays consist of large volume, highly segmented and position-sensitive HPGe detector crystals. After an intense development of this new technology over the past two decades, see *e.g.* refs. [1–24], a  $1\pi$  version of these arrays has been realised, namely GRETINA [1, 25] and the AGATA demonstrator [2]. These two arrays are currently used at state-of-the-art accelerator facilities in the USA and Europe with great success, see *e.g.* refs. [26–39]. New detector modules are being continuously added to these arrays with the ultimate goal of reaching a  $4\pi$  geometry and forming GRETA (Gamma Ray Energy Tracking Array) and AGATA (Advanced GAMMA Tracking Array). The advantages of such arrays over previous generations of HPGe arrays and the new scientific programme that they enable have been discussed extensively in refs. [7,

15]. Despite the very successful scientific programme that these arrays have already enabled, achieving their optimum performance in terms of  $\gamma$ -ray tracking remains a challenge.

The  $\gamma$ -ray energy tracking technique requires a precise knowledge of the  $\gamma$ -ray interaction positions inside the detector volume and the energy deposited in each interaction. Tracking, *i.e.* finding the true sequence of interaction positions of a given  $\gamma$ -ray, is performed by grouping and ordering these interactions utilising geometrical criteria and the Compton scattering formula, see *e.g.* ref. [40] for details. The three-dimensional interaction positions, that are needed for tracking, are obtained through electrical segmentation of the detector's outer electrodes and through pulse-shape analysis of the recorded electronic signals; indeed, the shape of the signals induced at the electrodes is position dependent [12]. Currently the most effective way to extract the  $\gamma$ -ray interaction positions from the signal pulse shapes is a comparison of the measured signals against a library of expected pulse shapes corresponding to different  $\gamma$ -ray interaction positions within the detector volume. This library of signals is hereafter referred to as *signal basis*. The signal basis typically contains a dense grid of predefined points and the associated signals expected to originate from a  $\gamma$ -ray interaction at these given points. Interpolation of the signals between the points of the grid allows for a continuous representation of the entire detector volume. The problem of position reconstruction

<sup>a</sup> e-mail: stefanos.paschalis@york.ac.uk

<sup>b</sup> e-mail: marina.petri@york.ac.uk

is then reduced into producing a reliable signal basis and comparing efficiently the measured and expected signals in real time.

The methods for generating a signal basis can be distinguished into experimental and analytical ones. In practice, a combination of experimental and analytical methods is used to generate the signal bases that are currently being used with the  $\gamma$ -ray energy tracking arrays.

With the experimental approaches, one performs an exhaustive scanning of the crystal volume with dedicated scanning setups (hence *in vitro* measurements) and generates a signal basis from the average of the measured signals in each scanned position, see *e.g.* refs. [3–6, 8, 22, 41–44]. Such experimental methods have the advantage that the basis is generated without the need of an in-depth understanding and control of all the factors that determine the shape of the generated signals. Common drawback to all experimental methods is the long acquisition time required to perform the scans for all detector modules and that the experimental conditions could be different between the signal basis generation process and the actual experiment. For example, the electronics' noise level could be different during scanning and the actual in-beam experiment; in addition, any uncertainty in the mechanical alignment during the detector scanning can cause systematic deviations in the produced signal basis.

In analytical methods, a calculated signal basis is produced based on electric field simulations and signal generation algorithms, see *e.g.* ref. [45]. The steps for such calculations include solving the Poisson equation for the given geometry and applied voltage, taking into account the intrinsic space-charge density, the electron/hole mobility, crystal temperature and crystal orientation. The accuracy of these estimated signals depends on the precise knowledge of these factors and an accurate modeling of their influence on the shape of the signal. The accurate modeling of the signals requires also detailed knowledge of the passivated and contact thicknesses and the actual shape of the charge cloud and its evolution as the charges drift inside the detector. In addition, the calculated signals must account also for the signal shaping caused by the front-end electronics and non-negligible cross-talk effects between the detector electronic channels.

A further challenge in producing a reliable signal basis of the detector signals is the possible time-dependent variations of the signal shape during operation *e.g.* due to radiation damage of the detector or electronic noise sources that may vary throughout an experimental campaign.

In this article, we discuss a novel experimental method to perform full characterization of all detectors in a  $\gamma$ -ray energy tracking array simultaneously and *in situ*. We show that a high-fidelity signal basis can be produced utilising the position sensitivity and  $\gamma$ -ray tracking capabilities of these arrays in an iterative way. Eventually, the fidelity of such signal-basis generation is shown to be limited only by statistics. The method has been tested thoroughly using Monte Carlo simulations (GEANT4) and realistic assumptions for the detector performance, while the relevance to

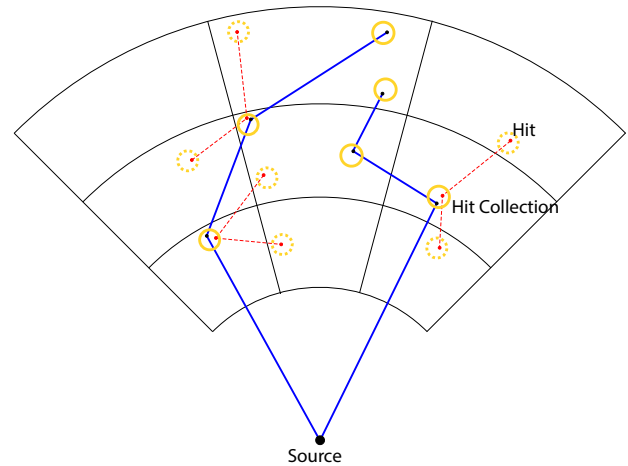


**Fig. 1.** Schematic representation of different  $\gamma$ -ray interactions in the detector volume. Groups of hits from different  $\gamma$ -ray events form the hit collections. The two exemplary tracks (blue solid line) consists of three hits. The hits of these two tracks belong to hit collections (yellow solid circle). These hit collections are connected to other hit collections (yellow dashed circle) by other tracks (red dashed lines).

an actual experimental implementation is also discussed where applicable.

## 2 Proposed method

A  $\gamma$ -ray source illuminates (without collimation) the full array, as it is done in a conventional  $\gamma$ -ray energy calibration run. The emitted  $\gamma$  rays interact with the crystal and then Compton scatter into neighboring detector regions where they interact again until being fully absorbed via a photoelectric effect. We start by grouping neighboring  $\gamma$ -ray interaction points (hereafter referred to as *hits*) originating from different  $\gamma$  rays into hit collections. Experimentally, this grouping can be achieved by comparing the recorded pulse shapes with each other. In simulations, the hit collections are formed using the simulated position of each hit; these positions are not used further, except for comparison to the final, converged result. Each hit collection is assigned a coarse position and during an iterative optimization (discussed below), their positions converge to their real positions with remarkable accuracy limited only by the acquired statistics.

The minimum size of the hit collection that can be used for grouping hits together reflects the position sensitivity of the detector, *i.e.* the signal variation between different positions compared to the noise level of the signals. This sensitivity alone is reported to be of the order of one millimeter or less depending on the detector region [23, 24]. However, the convergence depends strongly on the available number of hits within each hit collection. For the results presented in sect. 3, we have grouped hits that are located within a sphere of 5 mm diameter into the same hit collections, while we also show results for different hit collection sizes for comparison. Hits that happen

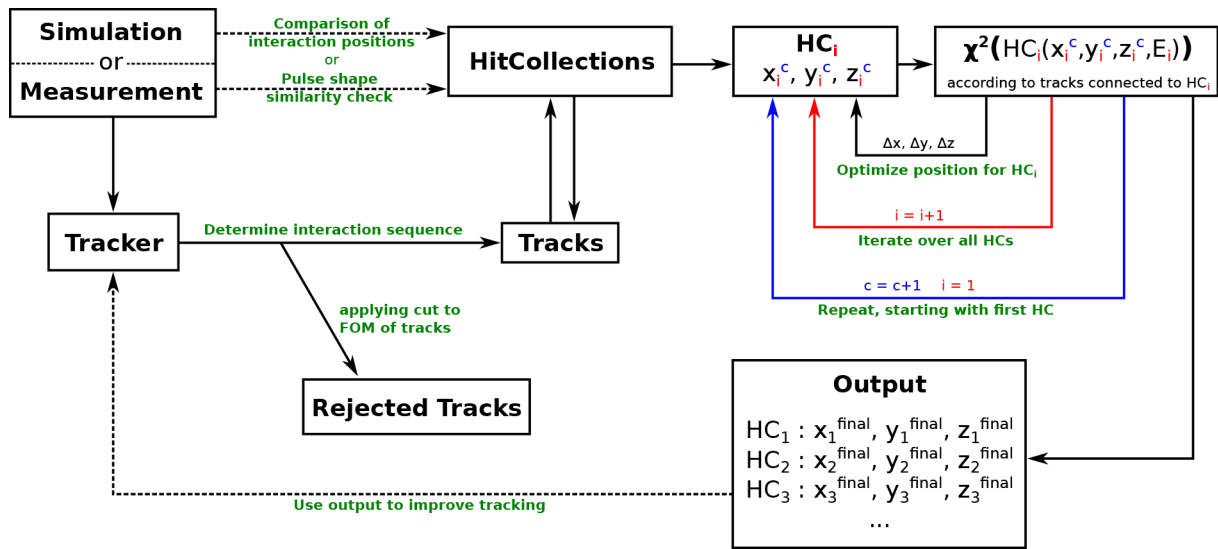


**Fig. 2.** The data used as input into the algorithm are either generated by simulation or by measurement. The hit collections (HC) are generated by comparing the simulated interaction positions or by performing a pulse shape similarity check, respectively. In addition, a tracking algorithm determines the most probable interaction sequence; the reconstructed tracks connect the hit collections. Applying a cut to the figure-of-merit (FOM) of the tracks can increase the fraction of correctly reconstructed tracks. A minimization algorithm is used to subsequently optimize the position of each hit collection  $i$  with respect to all other hit collections by taking into account the track information. Once every hit collection position has been optimized, the procedure is repeated starting again with the first hit collection. This is done repeatedly with every iteration  $c$  until a certain level of convergence (*e.g.*, defined by the change of positions between subsequent iterations) is reached. At this point, tracking can be repeated using the output of the position optimization algorithm to improve the tracking accuracy.

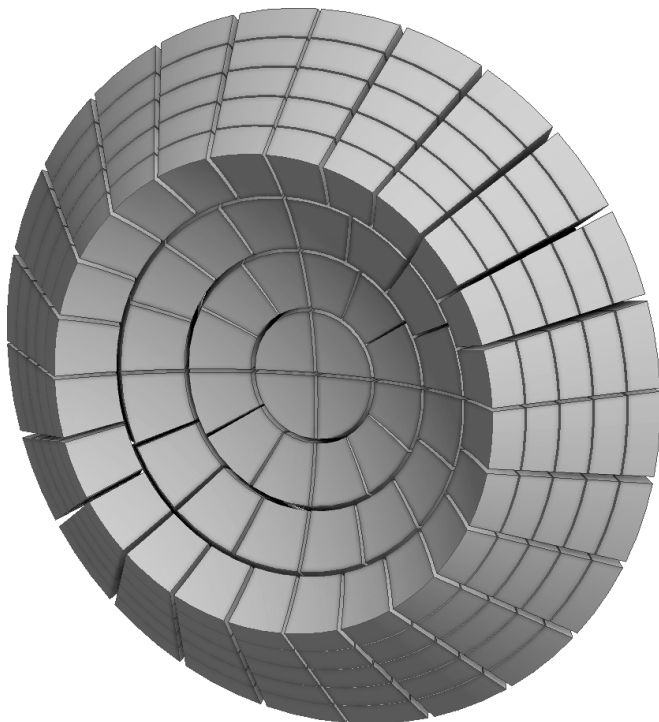


**Fig. 3.** A cut of a hollow sphere with an inner radius of 200 mm and an outer radius of 300 mm, covering an angular range of  $45^\circ$  in polar direction and the full  $360^\circ$  in azimuthal direction and a solid angle of  $0.586 \pi$  sr. The geometry is segmented into 5 radial segments, 4 segments in polar direction and 4, 12, and 24 segments in azimuthal direction, respectively.

to lie within multiple hit collections are assigned to all of them. A hit that cannot be assigned to an existing hit collection defines a new hit collection, which is then available for filling.

To reflect the real experimental conditions, the sequence of hits originating from a given  $\gamma$  ray is assumed to be unknown and a tracking algorithm is used to determine the most probable sequence of hits forming a  $\gamma$ -ray track using initially only the coarse positions of the hit collections containing the hits. The efficiency of such tracking algorithm in finding the correct sequence increases in every iteration as the positions of the hit collections containing the hits converge to their actual positions, further details of the observed performance are presented in sect. 3.

Following the initial  $\gamma$ -ray tracking, each hit residing in a hit collection is associated with hits in other hit collections via the determined track. In this way, each hit collection is linked (through its hits and their corresponding tracks) to multiple other hit collections. This process is illustrated in fig. 1.

At this stage we have a set of hit collections consisting of hits that lie close to each other. However, we do not know where exactly the hit collections are located in the detector volume and we assume that all hits belonging to a specific hit collection share the same position. Initially, the only position information available for a hit collection is the position of the segment where the  $\gamma$ -ray interaction took place; a nominal initial coarse position is thus assigned to the hit collection, *e.g.*, at the centre of the segment. The geometrical angles obtained for all tracks are compared to the respective Compton angles; the Compton

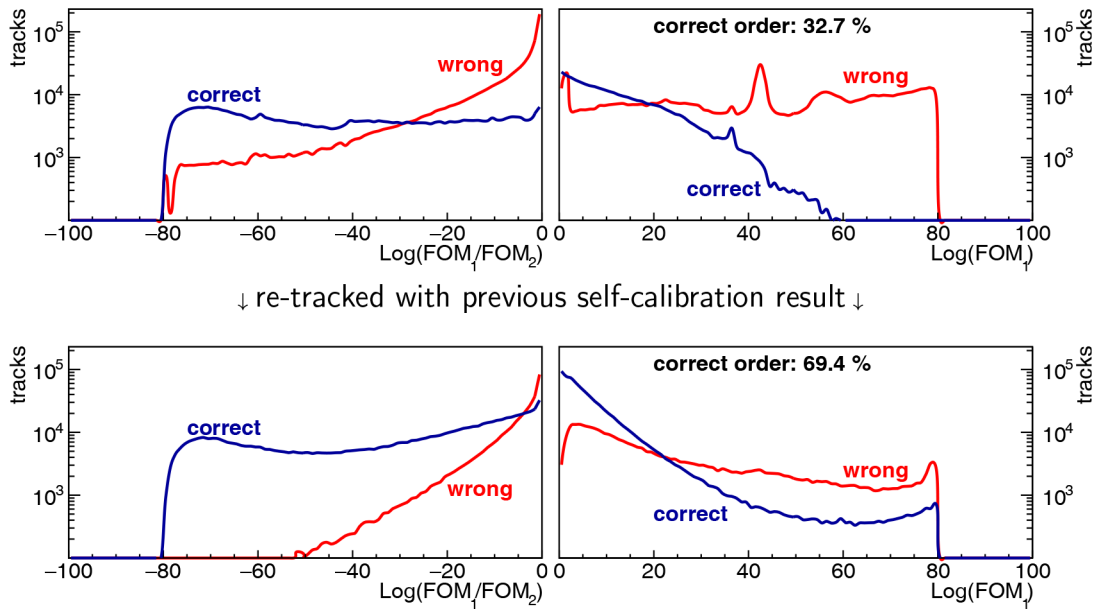


**Fig. 4.** Figure-of-merit (FOM) results of the tracking algorithm using the initial conditions (top) and using the results of the first self-calibration procedure (bottom). The right graphs show the abundance of tracks with a given FOM for the best interaction sequence ( $FOM_1$ ). The left graphs show the ratio of the best to the second best sequence ( $FOM_1/FOM_2$ ). They are shown separately for tracks where the interaction sequence has been determined correctly or not. For small values of  $FOM_1$  and  $FOM_1/FOM_2$  the sequences are predominantly correct. Thus, applying a cut allows to significantly improve the fraction of correctly reconstructed tracks. The peak structures in the top right plot are a result of the discretization induced by putting all the hit collections into the centre of segments. The structures indeed disappear when different starting conditions are used for the positions of the HC, as shown on the re-tracked plot (bottom right).

angle is calculated via the Compton scattering formula

$$\cos \alpha = 1 + \frac{m_e}{E_{\text{inc}}} - \frac{m_e}{E_{\text{inc}} - E_{\text{dep}}} \quad (1)$$

using the incident energy  $E_{\text{inc}}$  of the  $\gamma$  ray before the Compton scattering and the deposited energy  $E_{\text{dep}}$ . Iteratively, starting with one hit collection, the positions of all hit collections are adjusted such that the differences between geometrical and Compton angles are minimized. Although the positions were only roughly known at start, the large number and spatial distribution of the hit collections allows the minimization to obtain a new position closer to the real position. After the position of every hit collection has been optimized once, the first iteration (c) is completed and the procedure starts again with the first hit collection. With each iteration, the hit collection positions converge towards their real positions, which are evenly distributed throughout the detector volume. We note that a global minimization of all hit collections connected through all tracks simultaneously would give the result in a single iteration; however this is computationally challenging. The processes involved in this method are illustrated as a flow chart in fig. 2, while the results of the proposed method are summarised in sect. 3.

### 3 Results

To demonstrate the feasibility of the method, a fraction of a hollow sphere with an inner radius of 200 mm

and an outer radius of 300 mm, as shown in fig. 3, has been simulated; the solid angle coverage is  $0.586 \pi \text{ sr}$ . A  $\gamma$ -ray source is placed at the centre of the sphere emitting 2 MeV  $\gamma$  rays. For each interaction a realistic energy resolution is applied, typical for HPGe detectors, *i.e.*  $\Delta E(\text{in keV}) = \sqrt{1 + 3E(\text{in MeV})}$ . The GEANT4 physics list `G4EmStandardPhysics_option4`, in which the Doppler broadening caused by the electron's initial momentum is included, is used in the simulations. Interactions that are less than 2 mm apart have been merged into a single hit, since such interactions are not resolved in real experimental conditions.

For the initial conditions, *i.e.* using the centre of the segments as hit collection positions, the tracking algorithm determines the interaction sequence correctly in 32.7% of the cases (see fig. 4). Comparing the figure-of-merit (FOM) distributions<sup>1</sup> of the best  $\gamma$ -ray track ( $FOM_1$ ) and the second-best  $\gamma$ -ray track ( $FOM_2$ ) shows that by applying cuts to  $FOM_1$  and to the ratio of  $FOM_1$  and  $FOM_2$  the fraction of correct tracks can be significantly improved. For the results discussed in this section, these cuts ( $\log(FOM_1) < 20$  and  $\log(FOM_1/FOM_2) < -5$ ) improved the fraction of correct tracks from 32.7% to 83.5%, while reducing the total number of correct tracks by only about 50%. The obtained tracks (including the 16.5% wrongly reconstructed tracks) are then used in the position optimization.

<sup>1</sup> The FOM is the  $\chi^2$  of the tracking algorithm.

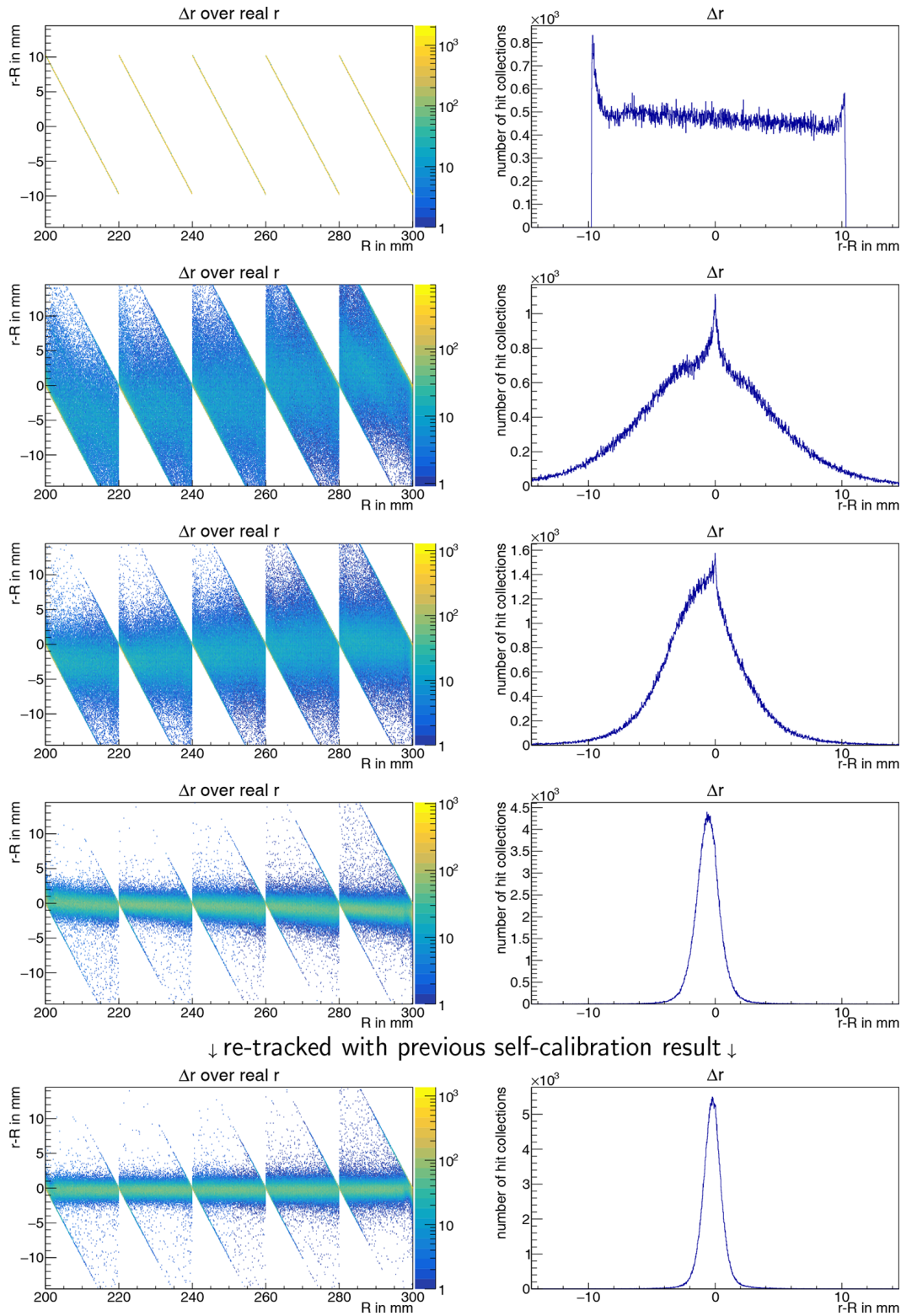


**Fig. 5.** Results of the self-calibration procedure as discussed in the text. The input data have been tracked. The left column shows the difference of the radii ( $\Delta r$ ) of the self-calibrated positions of the hit collections ( $r$ ) and the real radii of the positions of the hit collections ( $R$ ) plotted over  $R$ . The right column shows  $\Delta r$  for all hit collections. The first four rows have been tracked using the centre of the segments for the interactions. They show from top to bottom: Starting condition, after 1st iteration, after 2nd iteration and after 10th iteration. The last row shows results after the 10th iteration for data which have been re-tracked using the results of the previous self-calibration procedure. As a starting condition, all hit collections are placed in the centre of the corresponding segments. The resulting root-mean-square-deviation (RMSD) between the radius of the self-calibrated and real positions of the hit collections after 10 iterations is  $\text{RMSD} = 1.22 \text{ mm}$  and  $\text{RMSD} = 1.06 \text{ mm}$  after re-tracking. The systematic offset after 10 iterations is  $-0.59 \text{ mm}$  and  $-0.23 \text{ mm}$ , respectively.

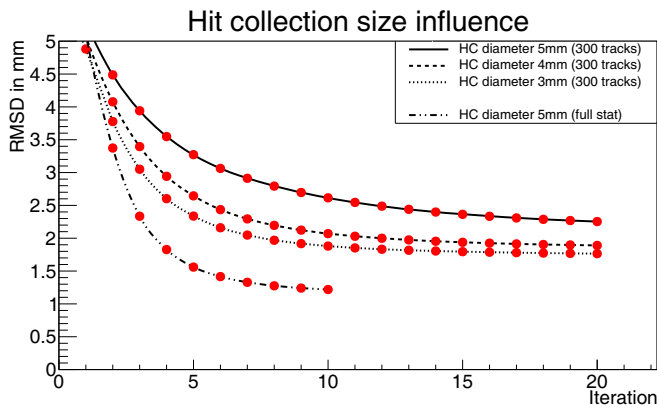


**Fig. 6.** Root-mean-square-deviation (RMSD) between the radius of the self-calibrated and real positions of the hit collections after each iteration for different hit collection (HC) diameters. The tracking was performed using the centre of the segments and figure-of-merit (FOM) considerations as described in sect. 3. For smaller hit collection diameters the RMSD improves slightly. A more significant improvement is achieved by increasing the number of tracks (statistics).

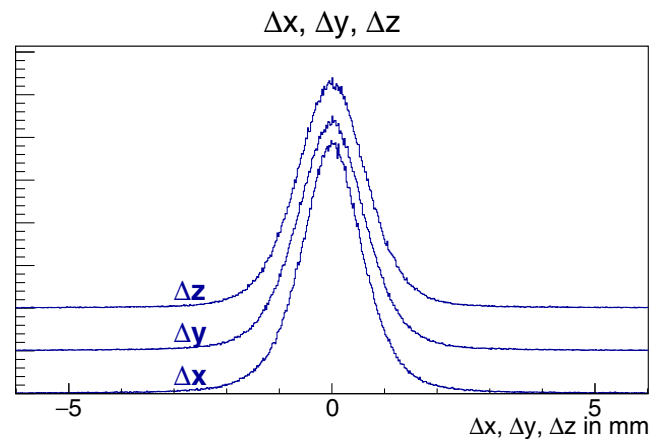
Figure 5 shows the results of the self-calibration for a hit collection of a 5 mm diameter sphere. The number of tracks connecting one hit collection to others ranges between 1000 and 3000 tracks per hit collection. To evaluate the results of the self-calibration the obtained positions of the hit collections are compared to their real positions. For the data which have been tracked using the centre of the segments, the root-mean-square-deviation (RMSD) between the radius of the self-calibrated and real positions of the hit collections after 10 iterations is  $\text{RMSD} = 1.22$  mm with a systematic offset of  $-0.59$  mm. For the data which have been tracked using the result of the previous self-calibration procedure,  $\text{RMSD} = 1.06$  mm with a systematic offset of  $-0.23$  mm after 10 iterations. The concept itself allows to further reduce the hit collection diameter and improve the achievable resolution.

Figure 6 shows a comparison of the convergence for different hit collection diameters and number of tracks. The RMSD between the radius of the self-calibrated and real positions of the hit collections improves for smaller hit collection diameters. A more significant improvement, however, is achieved with increasing number of tracks (statistics).

To complete the picture and extend the presented coordinates beyond the radius, fig. 7 summarizes the results of the self-calibration procedure after re-tracking the input data for hit collections of a 5 mm diameter sphere. The deviation of the determined hit collection position from the real position in Cartesian coordinates is  $\text{RMSD} = 1.0$  mm.

## 4 Outlook

Although the implementation of the proposed technique to existing  $\gamma$ -ray energy tracking arrays, *e.g.* GRETA and



**Fig. 7.** Self-calibration results for a hit collection diameter of 5 mm (10 iterations) after re-tracking the input data for Cartesian coordinates;  $\text{RMSD} = 1.0$  mm. The histograms have been shifted along the  $y$  axis for visibility.

AGATA, is beyond the scope of this article, we will discuss some key points as an outlook.

- 1) Experimentally, the number of hits within a segment is not known. Therefore, we have tested the robustness of the proposed method against the coalescence distance of two hits. The  $\chi^2$  obtained from the tracking algorithm is sensitive to the number of hits per segment and if coalescence has taken place, the  $\chi^2$  is in general worse. The FOM curves of fig. 8 show the behavior of the  $\chi^2$  in the extreme case when all hits occurring within a segment are merged and treated as one hit in that segment. The reconstructed FOM for these merged cases follow closely the wrongly reconstructed distribution. We conclude that the exact coalescence distance chosen is not affecting the principle of the technique.
- 2) Experimentally, there is a minimum energy deposited per hit below which the pulse-shape sensitivity is lost, *i.e.* the signal-to-noise ratio in the pulse shape is poor for low energy depositions (below few hundreds of keV). This effectively reduces the available statistics and increases the calibration time, discussed in sect. 4.1.
- 3) The suggested method can build on the huge progress that has already been made with the arrays, *i.e.* one could start from data that have been processed using current technology, and hits in neighbouring segments (or even the same segment) have been identified. Wrongly reconstructed hits can be flagged by the FOM, as discussed above.
- 4) The proposed technique is not restricted to data originating from a source measurement. Under certain experimental conditions, the use of in-beam data is possible and even advantageous; *e.g.* when high beam velocities are used, the energy of the Doppler-shifted  $\gamma$  ray restricts the spatial coordinates of the first interaction.

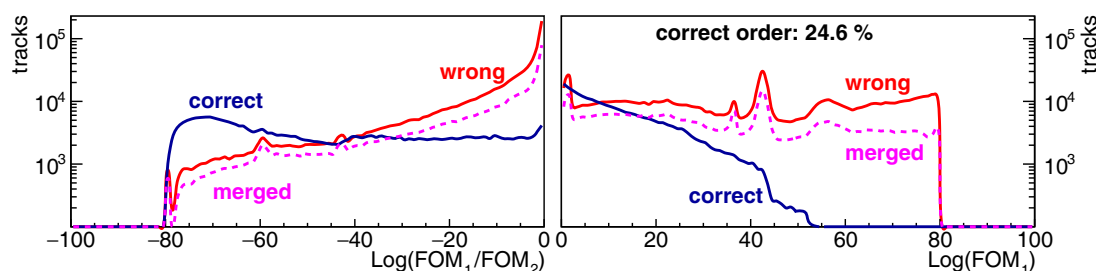


**Fig. 8.** Figure-of-merit (FOM) results of the tracking algorithm using the centre of segments as initial conditions. Interactions in the same detector segment have been merged. The right graph show the abundance of tracks with a given FOM for the best interaction sequence ( $FOM_1$ ). The left graphs show the ratio of the best to the second best sequence ( $FOM_1/FOM_2$ ). They are shown separately for tracks where the interaction sequence has been determined correctly or not. In addition, the dashed graph shows tracks where interactions have been merged. The behaviour for the merged tracks follows closely the general features of the wrongly tracked distribution. As such, applying cuts allows to predominantly exclude tracks with merged interactions.

#### 4.1 Timescales

Based on our analysis, an estimated hit density of about 20 hits per  $\text{mm}^3$  is sufficient to achieve robust convergence. In an actual experimental implementation of the proposed method, requiring at least 300 keV energy deposition per hit, a minimum distance of 20 mm between hits, and a single-crystal rate of a few kHz, one would need about 10 days of measurement time with a 1 MBq source. We emphasize that within this timescale the full array is calibrated.

With the current (not optimized) implementation of the self-calibration procedure, one iteration for a single crystal takes approximately 2.5 hours of CPU time on a Xeon E5-2690 at 2.90 GHz. This is a highly parallelizable procedure with minimal multithreading overhead; indeed, we typically used up to 56 cores that brings the time down to about 3 minutes per iteration per crystal. Currently, the memory requirement per crystal is around 30 GB, though significant optimizations are certainly possible and memory requirements can be reduced by a factor of three.

## 5 Conclusion

We have presented a novel technique to perform an *in situ* position calibration of  $\gamma$ -ray energy tracking arrays utilising a notably simple procedure. The primary input is the detector geometry, while no detailed knowledge of the electronic properties or detector response is required. The method delivers a signal basis with unprecedented fidelity, while keeping the required calibration times to a minimum. At the same time the method proves to be robust against all tested influences, including energy resolution, wrong interaction sequences, coalescence distance and low statistics. The presented method opens up the way for obtaining an optimum tracking performance, approaching the limits imposed by the sensitivity and the noise level of these  $\gamma$ -ray energy tracking arrays.

This work is supported by the Royal Society under contract number UF150476, the UK STFC under contract numbers ST/P003885/1 and ST/P001831/1, the Deutsche Forschungsgemeinschaft through SFB 1245 and the Helmholtz International Center for FAIR.

**Open Access** This is an open access article distributed under the terms of the Creative Commons Attribution License (<http://creativecommons.org/licenses/by/4.0>), which permits unrestricted use, distribution, and reproduction in any medium, provided the original work is properly cited.

## References

1. S. Paschalis *et al.*, Nucl. Instrum. Methods A **709**, 44 (2013).
2. S. Akkoyun *et al.*, Nucl. Instrum. Methods A **668**, 26 (2012).
3. N. Goel *et al.*, Nucl. Instrum. Methods A **652**, 591 (2011).
4. N. Goel *et al.*, Nucl. Instrum. Methods A **700**, 10 (2013).
5. C. Domingo-Pardo *et al.*, Nucl. Instrum. Methods A **643**, 79 (2011).
6. F.C.L. Crespi *et al.*, Nucl. Instrum. Methods A **593**, 440 (2008).
7. M.A. Deleplanque *et al.*, Nucl. Instrum. Methods A **430**, 292 (1999).
8. F.C.L. Crespi *et al.*, Nucl. Instrum. Methods A **705**, 47 (2013).
9. P.-A. Söderström *et al.*, Nucl. Instrum. Methods A **638**, 96 (2011).
10. T.J. Ross *et al.*, Nucl. Instrum. Methods A **606**, 533 (2009).
11. M. Descovich *et al.*, Nucl. Instrum. Methods A **545**, 199 (2005).
12. I.Y. Lee, M.A. Deleplanque, K. Vetter, Rep. Prog. Phys. **66**, 7 (2003).
13. J. Eberth, J. Simpson, Prog. Part. Nucl. Phys. **60**, 283 (2008).
14. John Anderson *et al.*, IEEE Trans. Nucl. Sci. **56**, 258 (2009).
15. I.Y. Lee *et al.*, Nucl. Phys. A **746**, 1 (2004).
16. I.Y. Lee, AIP Conf. Proc. **1139**, 23 (2009).
17. Sergio Zimmermann *et al.*, IEEE Trans. Nucl. Sci. **59**, 2494 (2012).
18. M. Descovich *et al.*, Nucl. Instrum. Methods A **241**, 931 (2005).
19. M. Cromaz *et al.*, Nucl. Instrum. Methods A **597**, 233 (2008).
20. Sergio Zimmermann, Dionisio Doering, in *IEEE International Conference on Acoustics, Speech and Signal Processing* (IEEE, 2010) p. 2794.

21. A.J. Boston *et al.*, Nucl. Instrum. Methods B **261**, 1098 (2007).
22. P. Desesquelles *et al.*, Nucl. Instrum. Methods A **729**, 198 (2013).
23. K. Vetter *et al.*, Nucl. Instrum. Methods A **452**, 105 (2000).
24. K. Vetter *et al.*, Nucl. Instrum. Methods A **452**, 223 (2000).
25. D. Weisshaar *et al.*, Nucl. Instrum. Methods A **847**, 187 (2017).
26. Paul Fallon, Alexandra Gade, I-Yang Lee, Annu. Rev. Nucl. Part. Sci. **66**, 321 (2016).
27. A. Mutschler *et al.*, Nat. Phys. **13**, 152 (2016).
28. Philip Walker, Nat. Phys. **10**, 338 (2014).
29. L. Pellegri *et al.*, Phys. Lett. B **738**, 519 (2014).
30. F.C.L. Crespi *et al.*, Phys. Rev. Lett. **113**, 012501 (2014).
31. S. Ceruti *et al.*, Phys. Rev. Lett. **115**, 222502 (2015).
32. K. Hadyńska-Klek *et al.*, Phys. Rev. Lett. **117**, 062501 (2016).
33. A. Gade *et al.*, Phys. Rev. Lett. **112**, 112503 (2014).
34. H. Iwasaki *et al.*, Phys. Rev. Lett. **112**, 142502 (2014).
35. S. Noji *et al.*, Phys. Rev. Lett. **112**, 252501 (2014).
36. C. Langer *et al.*, Phys. Rev. Lett. **113**, 032502 (2014).
37. K. Kolos *et al.*, Phys. Rev. Lett. **116**, 122502 (2016).
38. A.D. Ayangeakaa *et al.*, Phys. Lett. B **754**, 254 (2016).
39. B. Bucher *et al.*, Phys. Rev. Lett. **116**, 112503 (2016).
40. G.J. Schmid *et al.*, Nucl. Instrum. Methods A **430**, 69 (1999).
41. L. Nelson *et al.*, Nucl. Instrum. Methods A **573**, 153 (2007).
42. M.R. Dimmock *et al.*, IEEE Trans. Nucl. Sci. **56**, 1593 (2009).
43. A.J. Boston *et al.*, Nucl. Instrum. Methods A **604**, 48 (2009).
44. T.M.H. Ha *et al.*, Nucl. Instrum. Methods A **697**, 123 (2013).
45. B. Bruyneel, B. Birkenbach, P. Reiter, Eur. Phys. J. A **52**, 70 (2016).